PHYSICAL REVIEW D **95,** 052006 (2017)

Constraints on axion couplings from the CDEX-1 experiment at the China Jinping Underground Laboratory

S. K. Liu,[1,2] Q. Yue,[1,*] K. J. Kang,[1] J. P. Cheng,[1] H. T. Wong,[7,†] Y. J. Li,[1] H. B. Li,[7,†] S. T. Lin,[2,7] J. P. Chang,[5] J. H. Chen,[7,†] N. Chen,[1] Q. H. Chen,[1] Y. H. Chen,[6] Z. Deng,[1] Q. Du,[2] H. Gong,[1] H. J. He,[1] Q. J. He,[1] H. X. Huang,[3] H. Jiang,[1] J. M. Li,[1] J. Li,[1] J. Li,[5] X. Li,[3] X. Q. Li,[4] X. Y. Li,[4] Y. L. Li,[1] F. K. Lin,[7,†] L. C. Lü,[1] H. Ma,[1] J. L. Ma,[1] S. J. Mao,[5] J. Q. Qin,[1] J. Ren,[3] J. Ren,[1] X. C. Ruan,[3] V. Sharma,[7,8,†] M. B. Shen,[6] L. Singh,[7,8,†] M. K. Singh,[7,8,†] A. K. Soma,[7,8,†] J. Su,[1] C. J. Tang,[2] J. M. Wang,[6] L. Wang,[1,2] Q. Wang,[1] S. Y. Wu,[6] Y. C. Wu,[1] Y. C. Wu,[5] Z. Z. Xianyu,[1] R. Q. Xiao,[1] H. Y. Xing,[2] F. Z. Xu,[1] Y. Xu,[4] X. J. Xu,[1] T. Xue,[1] C. W. Yang,[2] L. T. Yang,[1] S. W. Yang,[7,†] N. Yi,[1] C. X. Yu,[4] H. Yu,[1] X. Z. Yu,[2] X. H. Zeng,[6] Z. Zeng,[1] L. Zhang,[5] Y. H. Zhang,[6] M. G. Zhao,[4] W. Zhao,[1] Z. Y. Zhou,[3] J. J. Zhu,[2] W. B. Zhu,[5] X. Z. Zhu,[1] and Z. H. Zhu[6]

(CDEX Collaboration)

[1]*Key Laboratory of Particle and Radiation Imaging (Ministry of Education) and Department of Engineering Physics, Tsinghua University, Beijing 100084*
[2]*College of Physical Science and Technology, Sichuan University, Chengdu 610064*
[3]*Department of Nuclear Physics, China Institute of Atomic Energy, Beijing 102413*
[4]*School of Physics, Nankai University, Tianjin 300071*
[5]*NUCTECH Company, Beijing 100084*
[6]*YaLong River Hydropower Development Company, Chengdu 610051*
[7]*Institute of Physics, Academia Sinica, Taipei 11529*
[8]*Department of Physics, Banaras Hindu University, Varanasi 221005*

(Received 24 October 2016; revised manuscript received 27 January 2017; published 30 March 2017)

We report the results of searches for solar axions and galactic dark matter axions or axionlike particles with the CDEX-1 experiment at the China Jinping Underground Laboratory, using 335.6 kg days of data from a p-type point-contact germanium detector. The data are compatible with the background model, and no excess signals are observed. Limits of solar axions on the model-independent coupling $g_{Ae} < 2.5 \times 10^{-11}$ from Compton, bremsstrahlung, atomic-recombination, and deexcitation channels and $g_{AN}^{\mathrm{eff}} \times g_{Ae} < 6.4 \times 10^{-17}$ from a ^{57}Fe M1 transition at 90% confidence level are derived. Within the framework of the Dine-Fischler-Srednicki-Zhitnitskiy and Kim-Shifman-Vainshtein-Zakharov models, our results exclude the axion mass heavier than 0.9 and 177 eV/c^2, respectively. The derived constraints for dark matter axions below 1 keV improve over the previous results.

DOI: 10.1103/PhysRevD.95.052006

I. INTRODUCTION

Quantum chromodynamics (QCD), universally believed to be the best theory describing strong interactions, contains the Θ term which could explicitly give a rise to a measurable *CP* violation such as a large neutron electric dipole moment. The experimental bound is about 10 orders of magnitude more stringent [1], resulting in an unnaturally small upper limit ($<10^{-10}$) to the Θ parameter. In order to solve this "strong *CP* problem," Peccei and Quinn postulated a new spontaneously broken symmetry that naturally and dynamically cancels *CP* violation in the strong interactions [2]. Weinberg [3] and Wilczek [4] later proposed that this new symmetry introduces a new pseudoscalar particle similar to neutral pions called the axion. This original axion with a symmetry-breaking scale of the order of the electroweak scale has been excluded by experiments (see [5,6], and references therein), whereas "invisible" axion models such as the nonhadronic Dine-Fischler-Srednicki-Zhitnitskiy (DFSZ) model [7,8] and the hadronic Kim-Shifman-Vainshtein-Zakharov (KSVZ) model [9,10] arising from a higher symmetry-breaking energy scale are still allowed. In addition, axionlike particles (ALPs) appearing in many models of physics beyond the Standard Model have similar properties to the QCD axions which may have couplings to electrons (g_{Ae}), photons ($g_{A\gamma}$), and nucleons (g_{AN}). Nevertheless, in general, the mass and couplings of ALPs are not directly related, making the corresponding parameter space larger, and do not necessarily solve the strong *CP* problem.

Several dark matter (DM) experiments aiming at the direct detection of weakly interacting massive particles (WIMPs) have reported axion search results [11–18]. These experiments mainly incorporate two detection mechanisms. The first is that axions from our Sun have couplings to photons ($g_{A\gamma}$) in detectors through the Primakoff effect, $a + Q \rightarrow Q + \gamma$ (Q stands for charged particles). These

---

[*] yueq@mail.tsinghua.edu.cn
[†] Participating as a member of the TEXONO Collaboration.

measurements utilize the Bragg diffraction effect in the crystal detectors [11,12,15] in which the intense electric field would enhance the interaction cross section. The axion-photon coupling $g_{A\gamma}$ from this process is independent of the axion mass, and these constraints on $g_{A\gamma}$ have the best sensitivities above 1 eV comparing with the helioscope experiment [19] and microwave cavity experiment [20]. The second is that solar axions and DM ALPs have couplings to electrons (g_{Ae}) in detectors through the axioelectric effect:

$$a + e + Z \rightarrow e + Z, \tag{1}$$

which is similar to the photoelectric effect with the absorption of an axion instead of a photon [11,13–18].

The China Dark Matter Experiment (CDEX) pursues direct searches of low-mass WIMPs and studies of double-beta decay in ^{76}Ge [21–25] toward the goal of a ton-scale germanium detector array [26] at the China Jinping Underground Laboratory (CJPL) [27]. CJPL is located in the Jinping traffic tunnel, Sichuan province, China, with a vertical rock overburden of more than 2400 m, providing a measured muon flux of 61.7 $\mathrm{y}^{-1}\,\mathrm{m}^{-2}$ [28]. A pilot measurement CDEX-0 with a germanium detector array with 20 g target mass, achieving the threshold of 177 eV, was reported [29]. The CDEX-1 experiment adopted one single module of the p-type point-contact germanium (pPCGe) detector with a fiducial mass of 915 g [30]. Phase I of the CDEX-1 measurement in the absence of an anti-Compton detector and prior to surface suppression based on 14.6 kg days of data was published with a threshold of 400 eV [31]. The phase-II measurements, featuring an anti-Compton detector and bulk surface discrimination (BSD), based on 53.9 [32] and 335.6 kg days of data [33] were reported. Both results strongly disfavor the allowed region implied by residual excess events from CoGeNT with an identical detector target.

We report the axion searches results from the CDEX-1 experiment based on an exposure of 335.6 kg days of data, which is the same data set as Ref. [33]. We focus on the g_{Ae} couplings from the solar axions and the galactic DM ALPs through the axioelectric effect of Eq. (1). Studies on the $g_{A\gamma}$ coupling are not pursued, since the Bragg diffraction methods are less sensitive and have larger systematic uncertainties.

II. AXION SEARCHES WITH CDEX-1

A. CDEX-1 setup and overview

The CDEX-1 experiment adopted one single module of the pPCGe detector at 994 g of mass [31–33]. A cylindrical NaI(Tl) crystal with a well-shaped cavity enclosing the cryostat of the pPCGe, whose threshold was about 5 keV, served as the anti-Compton (AC) detector. Events in coincidence with the AC detector were discarded to get rid of the γ-ray-induced background.

The p^+ point-contact electrode after a pulsed-reset feedback preamplifier generated three identical energy-related signals. These three outputs were fed into the shaping amplifiers at 6 μs (S_{p6}), 12 μs (S_{p12}) shaping time, and a timing amplifier (T_p), respectively. The outputs from $\mathrm{S}_{p6,12}$ provided the energy measurement and system trigger of the data acquisition system. Their dynamic ranges were limited to 12 keV to achieve the maximal signal-to-noise ratio and maximal information for low-energy events. The output from T_p recording the raw fast pulse shape was used to discriminate the bulk and surface events. The amplitude serves as an alternative energy estimator with the dynamic range extended to 20 keV. The energy resolution of T_p is worse than that of S_{p6}, with σ at 10.37 keV of 106 and 91 eV, respectively. In this analysis, the energy definitions and resolution functions below and above 12 keV were adopted from S_{p6} and T_p, respectively. An excellent linearity is observed, and its accuracy better than 0.8% is derived from the internal cosmogenic x-ray peaks and random trigger events in two channels [33].

B. Axion sources

1. Solar axions

The Sun can be an abundant source of axions, which are generated by four production mechanisms that depend on g_{Ae} [34]:

(i) Compton-like scattering (C): $\gamma + e \rightarrow e + a$;
(ii) axion bremsstrahlung (B): $e + Q \rightarrow e + Q + a$;
(iii) atomic recombination (R): $e + I \rightarrow I^- + a$;
(iv) atomic deexcitation (D): $I^* \rightarrow I + a$;

where Q is any charged particle, e is the electron, I is the ion, and I^* is its excited state.

The fluxes of all processes from Compton-like scattering, axion bremsstrahlung, atomic recombination and atomic deexcitation (CBRD) processes are estimated by Refs. [34,35], and as to the CB solar axions, the fluxes are

$$\begin{aligned}\frac{d\Phi_{\mathrm{CB}}}{dE_A} &= \frac{d\Phi_{\mathrm{C}}}{dE_A} + \frac{d\Phi_{\mathrm{B}}}{dE_A} \\ &= g_{Ae}^2 \times 1.33 \times 10^{33} E_A^{2.987} e^{-0.776 E_A} \\ &\quad + g_{Ae}^2 \times 2.63 \times 10^{35} E_A e^{-0.77 E_A} \frac{1}{1 + 0.667 E_A^{1.278}},\end{aligned} \tag{2}$$

where the unit is $\mathrm{cm}^{-2}\,\mathrm{s}^{-1}\,\mathrm{keV}^{-1}$ and axion energy E_A is in keV. For RD solar axions, the flux also depends on g_{Ae}^2, and the tabulated spectrum in Ref. [35] is adopted. As discussed in Ref. [35], the most recent and accurate calculation for solar axion flux is valid for light axions; hence, we consider only the axion mass $m_A < 1\ \mathrm{keV}/\mathrm{c}^2$.

The 14.4 keV monochromatic axions emitted in the M1 transition of ^{57}Fe nuclei in the Sun,

$$^{57}\mathrm{Fe}^* \to {}^{57}\mathrm{Fe} + a, \tag{3}$$

can be an additional important source of solar axions due to the large abundance of ^{57}Fe among the heavy elements [36,37]. Its flux is related to g_{AN} coupling and is given by [15,38]

$$\Phi_{14.4} = \left(\frac{k_A}{k_\gamma}\right)^3 \times 4.56 \times 10^{23} (g_{AN}^{\mathrm{eff}})^2, \tag{4}$$

where the unit is cm^{-2} s^{-1} and k_A and k_γ are the momenta of the outgoing axion and photon, respectively. The effective nuclear coupling g_{AN}^{eff} is model dependent, $g_{AN}^{\mathrm{eff}} \equiv (-1.19 g_{AN}^0 + g_{AN}^3)$, where g_{AN}^0 and g_{AN}^3 are the model-dependent isoscalar and isovector axion-nucleon coupling constants, respectively [39,40].

2. Galactic DM ALPs

The nonthermal axions or ALPs, produced by the vacuum realignment mechanism and radiation from cosmic strings, are candidates to solve the dark matter problem in the Universe. The total average flux independent of any axion coupling is given by

$$\Phi_{\mathrm{DM}} = \rho_{\mathrm{DM}} \cdot v_A / m_A$$
$$= 9.0 \times 10^{15} \times \beta \cdot \left(\frac{\mathrm{keV}}{m_A}\right) \ \mathrm{cm}^{-2}\,\mathrm{s}^{-1}, \tag{5}$$

where ρ_{DM} is the dark matter halo density ($\rho_{\mathrm{DM}} \sim 0.3\ \mathrm{GeV/cm}^3$ [41]), m_A is the axion mass, v_A is the mean axion velocity distribution with respect to Earth, and β is the ratio of the axion velocity to the speed of light.

C. Experimental signatures

We focus on the detection channel of axioelectric effect as illustrated in Eq. (1), where the cross section σ_{Ae} is given by

$$\sigma_{Ae}(E_A) = \sigma_{pe}(E_A) \frac{g_{Ae}^2}{\beta} \frac{3E_A^2}{16\pi\alpha m_e^2} \left(1 - \frac{\beta^{\frac{2}{3}}}{3}\right) \tag{6}$$

as described in Refs. [42–44], where $\sigma_{pe}(E_A)$ is the photoelectric cross section for Ge, α is the fine structure constant, m_e is the electron mass, and β is the ratio of the axion velocity to the speed of light.

The expected axion event rate at measurable energy E is obtained by the convolution of the flux, the axioelectric cross section, and the energy resolution of the detector:

$$R_i(E) = \int dE_A \sigma_{Ae}(E_A) \left(\frac{d\Phi_i}{dE_A}\right) \times \frac{1}{\sqrt{2\pi}\sigma} e^{-\frac{(E-E_A)^2}{2\sigma^2}}, \tag{7}$$

where i represents the different axion sources of fluxes Φ_i. The detector energy resolution (σ) is 91 eV at 10.37 keV [33].

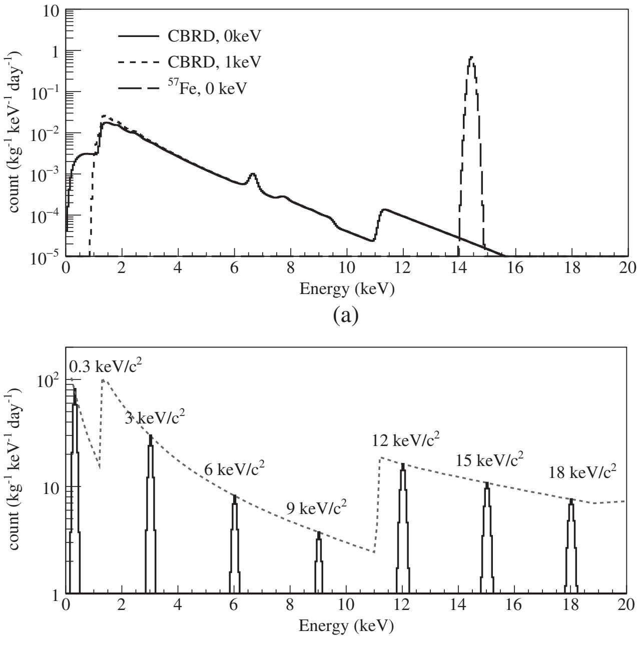

(a)

(b)

FIG. 1. The expected axion event rates in the CDEX-1 detector with energy resolution. (a) Solar axions: solid line, CBRD axion at the mass close to 0 keV; dotted line, CBRD axion at the mass of 1 keV; dashed line, ^{57}Fe 14.4 keV axion at the mass of 0 keV. (b) The dashed line is the maximum event rate of DM ALP Gaussian distributions vs their masses. The signal signatures as shown in solid lines are Gaussian distributions with the width determined by the energy resolution and the maximum point described by the dashed line. Here the axion couplings are $g_{Ae} = 10^{-11}$ and $g_{AN}^{\mathrm{eff}} \times g_{Ae} = 10^{-16}$.

In particular, since the ALP DM is cold ($\beta \approx 10^{-3}$), Eq. (7) translates to [44]

$$R = 1.2 \times 10^{43} A^{-1} g_{Ae}^2 m_A \sigma_{pe}(m_A), \tag{8}$$

where A is the mass number for germanium and the units of R and σ_{pe} are kg^{-1} day^{-1} and barns/atom, respectively. We note that the sensitivity dependence on the coupling strength is different for different sources and detector channels. The event rate $R_i(E)$ varies as g_{Ae}^4, $(g_{Ae} \times g_{\mathrm{AN}}^{\mathrm{eff}})^2$, and g_{Ae}^2 for $i =$ CBRD, ^{57}Fe, and DM, respectively. The difference in the coupling dependence of ALP DM rates compared to those of solar axions is a consequence of the DM flux being fixed by astrophysical data given a certain m_A. The expected $R_i(E)$ for various channels in CDEX-1 are depicted in Fig. 1.

III. DATA ANALYSIS

A. Candidate event selection

The background spectrum is derived by the same selection procedures used in earlier analysis [32,33]:

(i) stability check, which discards the time periods of calibration or laboratory construction;

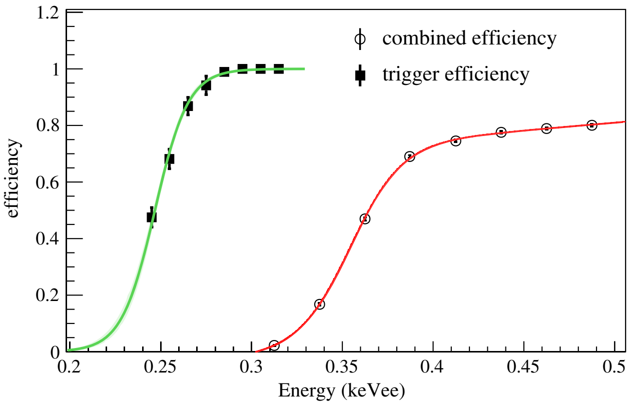

FIG. 2. Trigger efficiency as well as the combined efficiency (ϵ_{BC}) including trigger efficiency, physics vs electronic noise selection efficiencies, and anti-Compton selection efficiency.

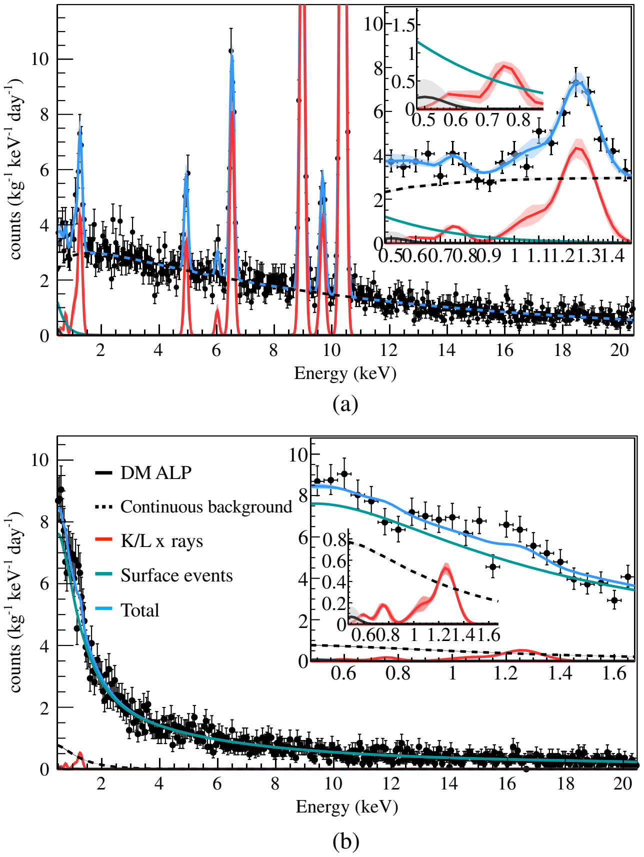

(a)

(b)

FIG. 3. The spectra of bulk measurement (a) B_m and surface measurement (b) S_m, respectively. The insets focus on the low-energy range. The solid black line is the best fit of the DM ALP expected spectrum at 500 eV/c^2 which corresponds to the P_α in B_0. The red line is K/L shell x rays which corresponds to the $P_{K,L}$ in B_0. The dashed black line is the continuous background which corresponds to the global exponential background P_{bkg} in B_0. The green line is the surface events which correspond to the P_{S_0} in S_0. The blue line is the combined spectrum of all these four components. The uncertainty bands at $\pm 1\sigma$ are also shown for the DM ALP and K/L x-ray spectra. The uncertainties of the other components are negligible on this scale.

(ii) physics vs electronic noise, which differentiates physical events from the electronic noise and spurious signals;

(iii) anti-Compton selection, which removes the events in coincidence with the anti-Compton detector.

In particular, there exists an inactive layer of about 1 mm in thickness at the n^+ surface electrode. These surface events are rejected by pulse shape analysis using their characteristic slower rise time [32,33]. Procedures have been established to derive their signal-retaining and background-leakage efficiencies [45].

Depicted in Fig. 2 are the trigger efficiency as well as variations of combined efficiencies (ϵ_{BC}) with energy, including those from the trigger, selection of physics vs electronic noise events, and anti-Compton vetos. The trigger efficiency is derived by the calibration sources in coincidence with the AC detector [29,32,33]. The selection efficiencies are derived by events due to random triggers [31,32] and the ^{241}Am calibration source. The analysis threshold of this work is chosen to be 325 eV, where the combined efficiency is 17%. The BSD are applied only for events above 475 eV.

B. Background description and background model simplification

In this work, we analyze the same data set as Ref. [33] with an exposure of 335.6 kg days of data. Every measured event is categorized as a bulk or surface event as the black data points shown in Fig. 3 from 475 eV, denoted by B_m and S_m, respectively, according to its rise time. The relationships between the measured spectrum (B_m, S_m) and the efficiency-corrected spectrum (B_0, S_0) can be derived from the following coupled equations, which are illustrated in Refs. [32,33,45]:

$$\begin{aligned} B_m &= \epsilon_{BC} \cdot [\epsilon_{BS} \cdot B_0 + (1 - \lambda_{BS}) \cdot S_0], \\ S_m &= \epsilon_{BC} \cdot [\lambda_{BS} \cdot S_0 + (1 - \epsilon_{BS}) \cdot B_0]. \end{aligned} \tag{9}$$

ϵ_{BC} refers to the combined efficiencies mentioned in Sec. III A. The efficiencies of ϵ_{BS} and λ_{BS}, representing the bulk event retaining and surface background rejection, can translate (B_m, S_m) to (B_0, S_0).

The B_0 and S_0 spectra (black dots) after the data selection including BSD described above and after the efficiency correction are shown in Fig. 4, as well as the efficiency-corrected spectrum (blue dots) without BSD from 300 eV up to 20 keV. The background consists of six distinct K-shell x-ray peaks from the cosmogenic nuclides and their corresponding L-shell x rays and a continuous component with a smooth, slightly increasing profile as the energy decreases [32,33].

The contribution of the ambient radioactivity at CJPL external to the shielding system was greatly suppressed to $\ll 10^{-6}$ kg^{-1} keV^{-1} day^{-1} at the energy range below

20 keV [33]. The continuous background below 20 keV was expected to mainly originate from residual ^{238}U, ^{232}Th, and ^{40}K in the experimental hardware in the vicinity of the *p*PCGe detector, radon gas penetrating inside shielding, and cosmogenic ^{3}H inside the crystal. Quantitative studies of their relative contributions are our current research efforts and beyond the scope of this work.

However, all the axion signals have signatures which are significantly different from the continuous background especially in the local energy range. As shown in Fig. 1, for ^{57}Fe solar axions and DM ALPs, compared with a continuous background, these event signatures are monochromatic and Poisson distributions whose widths are determined by the energy resolution. As to the continuous CBRD solar axion, the event rate has the distinct signature that it has a sawtoothlike profile between the local energy from 0.9 to 1.6 keV if we consider only the mass within 1 keV/c^2.

The accurate quantitative study of the continuous background is not essential for this axion sensitivity experiment. Therefore, we interpret the background in a simplified way: the combination of K/L x-ray peaks and a continuous background. A constant background within a local energy range of interest is sufficient for this analysis. The formulation of the analysis algorithms and evaluation of systematic uncertainties are discussed in subsequent sections.

C. Analysis method

The unbinned maximum likelihood method [11,17,18] is adopted to derive constraints in axion couplings from the measured spectrum. The best-fit solution to B_0 and S_0 is evaluated by maximizing the likelihood function [46]:

$$\mathcal{L} = \prod_{i=1}^{N_{B_m}} P_{B_{m_i}} \cdot \prod_{j=1}^{N_{S_m}} P_{S_{m_j}}, \tag{10}$$

where N_{B_m} and N_{S_m} are the numbers of bulk measurement events and surface measurement events, respectively. P_{B_m} and P_{S_m} are the probability density functions (PDFs) of the bulk measurement and surface measurement, respectively, which are described by

$$\begin{aligned} P_{B_m} = \varepsilon_{BC} \cdot [\varepsilon_{BS} \cdot (\alpha_{bkg} \cdot P_{bkg} + \alpha_{K,L} \cdot P_{K,L} \\ + \alpha_A \cdot P_A) + (1 - \lambda_{BS}) \cdot \alpha_{S_0} P_{S_0}], \end{aligned} \tag{11}$$

$$\begin{aligned} P_{S_m} = \varepsilon_{BC}[(1 - \varepsilon_{BS}) \cdot (\alpha'_{bkg} \cdot P_{bkg} + \alpha'_{K,L} \cdot P_{K,L} \\ + \alpha'_A \cdot P_A) + \lambda_{BS} \cdot \alpha'_{S_0} P_{S_0}]. \end{aligned} \tag{12}$$

According to the previous discussion of a simplified background model, the first background component P_{bkg} represents the normalized PDF of the continuous background. The other component, $P_{K,L}$, is the normalized PDF of the K/L shell x-ray peaks. P_A is the normalized PDF describing the axion events as shown in Fig. 1.

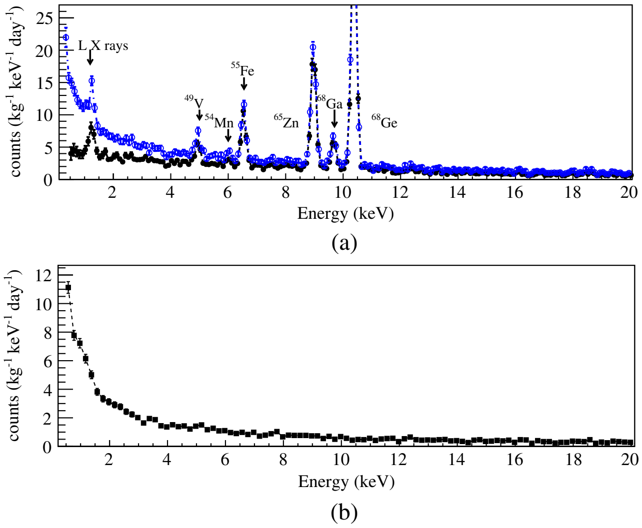

(a)

(b)

FIG. 4. (a) The efficiency-corrected bulk spectrum B_0 (black dots) from 475 eV up to 20 keV, as well as the efficiency-corrected total spectrum ($B_0 + S_0$) without BSD from 300 eV up to 20 keV. (b) The efficiency-corrected surface spectrum S_0.

P_{S_0} represents the normalized PDF of the efficiency-corrected surface spectrum S_0 in Fig. 4(b), derived from fitting S_0 by a smooth curve. The systematic uncertainties of the PDF selection of P_{S_0} is negligible by comparing bin by bin PDFs from the S_0 spectrum.

α_{bkg}, $\alpha_{K,L}$, α_A, and α_{S_0} are the relative contributions of each component in the bulk measurements, while α'_{bkg}, $\alpha'_{K,L}$, α'_A, and α'_{S_0} are their individual relative contributions to the surface measurements. Equations (11) and (12) are not independent and linked up with Eq. (13):

$$\alpha_i/\alpha'_i = C_i, \tag{13}$$

where C_i is cataloged and defined as follows:

$$C_i = \frac{\int \varepsilon_{BC}\varepsilon_{BS} P_i dE}{\int \varepsilon_{BC}(1 - \varepsilon_{BS}) P_i dE}, \qquad i = bkg, \quad K/L, A, \tag{14}$$

$$C_i = \frac{\int \varepsilon_{BC}(1 - \lambda_{BS}) P_{S_0} dE}{\int \varepsilon_{BC}\lambda_{BS} P_{S_0} dE}, \qquad i = S_0. \tag{15}$$

As demonstrated, the best simultaneous fit results of galactic DM ALPs at the mass of 500 eV/c^2 are shown in Fig. 3(a) of the bulk measurement and Fig. 3(b) of the surface measurement, using the exponential background. The solid black lines are the best fit of axion events, the red lines are the K/L shell x-ray events, and the green lines are the surface events.

The goodness of fit of this maximum likelihood analysis is tested with the binned data, where $\chi^2/n_d = 1.1$ (n_d represents the degrees of freedom) at the energy of 500 eV/c^2 of DM ALPs.

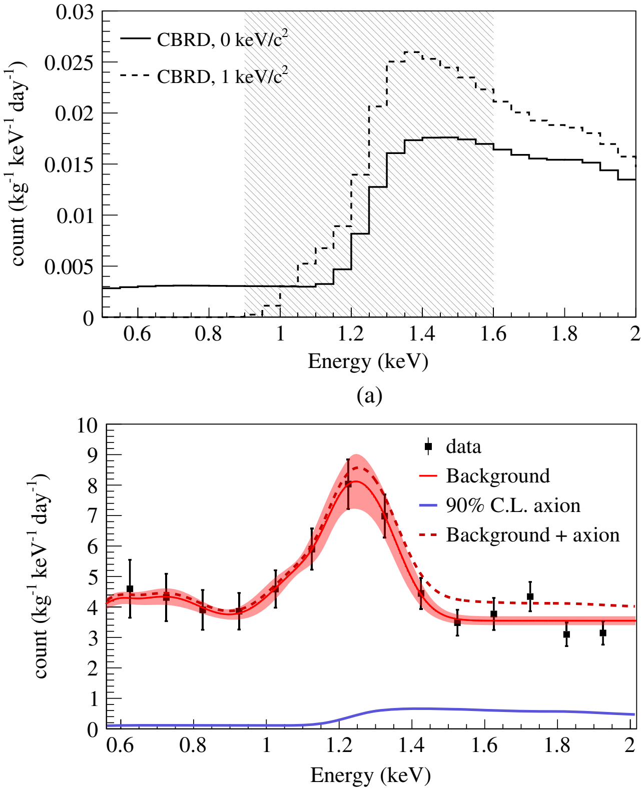

(a)

(b)

FIG. 5. (a) The expected axion rates in the CDEX-1 detector at the mass of 0 and 1 keV/c^2. (b) The 90% C.L. CBRD axion result at a mass of zero (blue line) and the B_0 spectrum (black data points) in the 0.475–2 keV energy range, as well as the background assumption (red line) and background +90% C.L. axion signal (dashed red line).

D. Systematic uncertainties

The effects of systematic uncertainties have been evaluated for all analyses from the three different axion sources. Systematic uncertainties may originate from bulk surface event selection, signal selection, and fiducial mass as well as the background assumption.

According to the evaluation in the previous work [33], the contribution of the uncertainty of bulk surface event selection in the low-energy range is dominated. This component has been taken into account in the likelihood function of Eq. (10) and introduced via the uncertainties of ε_{BS} and λ_{BS} in Eq. (9). This contributes about 48%, 15%, and well below 1% systematic uncertainties to the up limits of g_{Ae} couplings on galactic DM ALPs above 500 eV/c^2 and below 1 keV/c^2, the CBRD solar axion, and the ^{57}Fe solar axion, respectively.

The uncertainties of the background assumption P_{bkg} have been evaluated by the different background assumptions between the global exponential background, the local flat background, and the local polynomial background. The local fitting range is constrained by different kinds of axion sources. As to the CBRD solar axion, the fitting range is limited to 0.9–1.6 keV as shown in Fig. 5(a); for ^{57}Fe, that is limited to 13.0–16.0 keV as depicted in Fig. 7; and to the ALP DM axion, the range is constrained to the $\pm 8\sigma$ range. A locally constant background model is selected for the analysis, since this is adequate to provide good fits. Possible deviations in the real background profiles are integrated into the systematic uncertainties, which lead to changes in the upper limits of g_{Ae} couplings by about 8%, 5%, and 8% for the galactic DM ALPs between 500 eV/c^2 and 1 keV/c^2, the CBRD solar axion, and the ^{57}Fe solar axion, respectively.

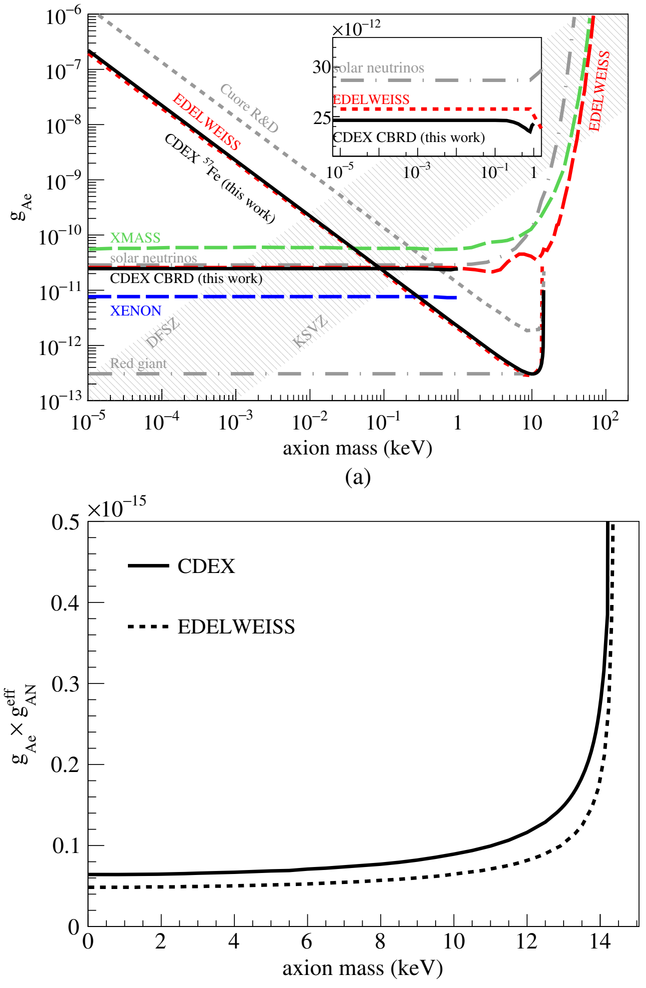

(a)

(b)

FIG. 6. (a) The CDEX-1 90% C.L. on the CBRD solar axion (solid black line) and the ^{57}Fe 14.4 keV solar axion (dashed black line) in the DFSZ model with $S = 0.5$ and $\cos^2\beta_{\mathrm{DFSZ}} = 1$, together with the bounds from astrophysical bounds [47–49], others including the CBRD axion and the ^{57}Fe axion [14–18]. The benchmark DFSZ ($\cos^2\beta_{\mathrm{DFSZ}} = 1$) and KSVZ ($E/N = 0$) models are displayed as two solid black lines. (b) The CDEX-1 90% C.L. on the model-independent coupling of $g^{\mathrm{eff}}_{AN} \times g_{Ae}$ of the ^{57}Fe 14.4 keV solar axion, compared with the EDELWEISS results [15].

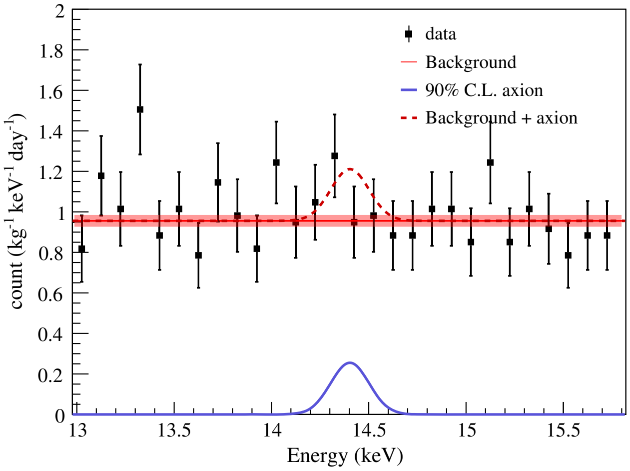

FIG. 7. The B_0 spectrum (black data points) and the 90% C.L. ^{57}Fe axion result (blue line) in the 13–16 keV energy range, as well as the background assumption (red line) background +90%C.L. axion signal (dashed red line).

Compared to the uncertainties arisen from bulk surface event selection and the background assumption, the contributions of the signal selection, fiducial mass, and energy resolution uncertainties of the detector to the systematic uncertainties are negligible.

IV. RESULTS

A. Solar axions

1. CBRD

For the CBRD solar axion, the sawtooth signature is within the energy range as the shadow displayed in Fig. 5(a), since we consider only the mass below 1 keV/c^2. The local fitting range is limited to the shadow region 0.9–1.6 keV, and the fitting results of 90% C.L. at the mass of 0 keV are shown in Fig. 5(b), as well as the B_0 spectrum and the background model described. The data are compatible with the background model, and no excess signals are observed. The solid black line in Fig. 6(a) shows our limit on g_{Ae} at 90% C.L., which is restricted to the mass below 1 keV/c^2, together with the bounds from astrophysical bounds [47–49] and other representative experiments including the CBRD axion and the ^{57}Fe axion [14–18].

As illustrated in the inset in Fig. 6(a), the improved energy threshold of CDEX-1 gives rise to a 90% C.L. limit of 2.5×10^{-11} for g_{Ae}, which is comparable to that of the EDELWEISS experiment [15], which also adopts germanium detectors.

As to a specific axion model, DFSZ or KSVZ [7–10], the g_{Ae} limit can be translated into the limit of axion mass m_A. In the DFSZ model, on the assumption of model-dependent parameter $\cos\beta_{\mathrm{DFSZ}} = 1$, where β_{DFSZ} is an arbitrary angle, CDEX-1 excludes axion masses above 0.9 eV/c^2. In the KSVZ model, on the assumption of model-dependent parameters $E/N = 0$, where E/N is the ratio of the electromagnetic to color anomalies of the Peccei-Quinn symmetry [40], our result excludes axion masses above 265 eV/c^2.

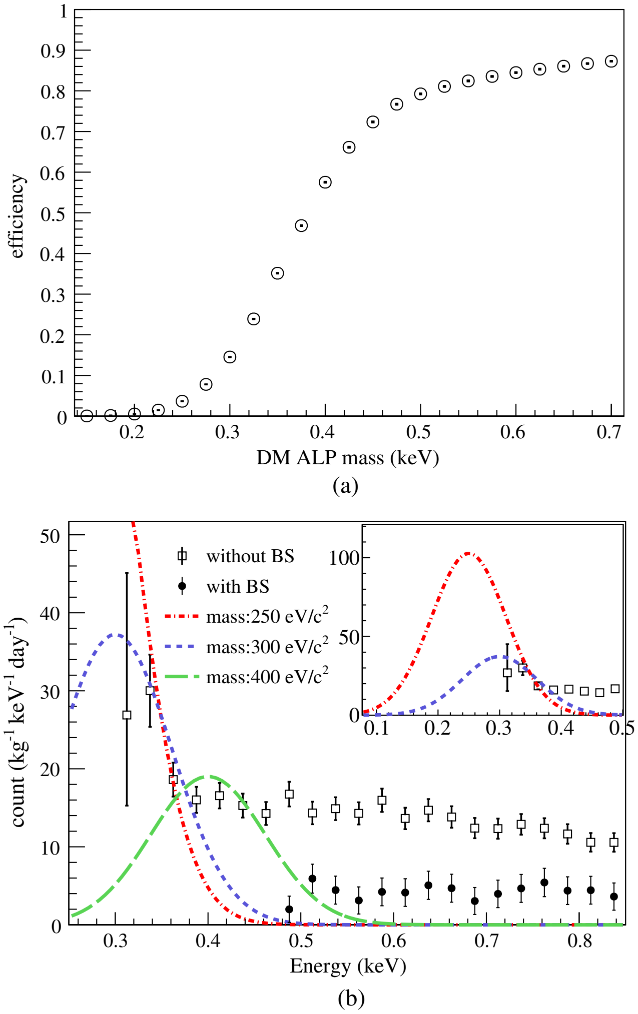

(a)

(b)

FIG. 8. (a) The variation of the detected signal efficiencies vs DM ALP mass at the analysis threshold of 325 eV. (b) The efficiency-corrected energy spectrum with and without BSD. The DM ALP spectra excluded at 90% C.L. for masses of 250, 300, and 400 eV/c^2 are superimposed. The inset shows an expanded vertical scale.

2. ^{57}Fe

For the ^{57}Fe M1 transition 14.4 keV axion, Fig. 7 displays the B_0 spectrum at the energy range of 13–16 keV as well as the background model. There is no hint of a line at 14.4 keV, and the expected signal at 90% C.L. is shown as the blue line. The model-independent limit of $g_{AN}^{\mathrm{eff}} \times g_{Ae} = 6.4 \times 10^{-17}$ is shown in Fig. 6(b) compared with the EDELWEISS limits [15]. The g_{AN}^{eff} is model-dependent coupling. In KSVZ models, it depends on the flavor-singlet axial-vector matrix element S [50,51]. In

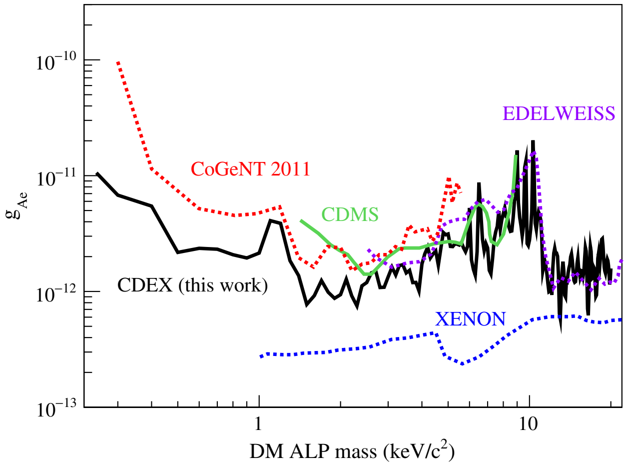

FIG. 9. The CDEX-1 90% C.L. on galactic DM ALP (black line), together with the bounds from other representative experiments [11,13,15,17,18].

DFSZ models, besides element S it also depends on the $\tan\beta_{\mathrm{DFSZ}}$, which is the ratio of two Higgs vacuum expectation values of the model. The dashed black line in Fig. 6(a) shows the 90% C.L. limit at the DFSZ model with $S = 0.5$ and $\cos^2\beta_{\mathrm{DFSZ}} = 1$. In the DFSZ and KSVZ models, using the parameters described above, the axion mass can be constrained to 9 and 177 eV/c^2, respectively. Combining the results from the CBRD channel and ^{57}Fe channel, our results exclude an axion mass heavier than 0.9 and 177 eV/c^2 according to the DFSZ and KSVZ model, respectively.

B. Galactic DM ALPs

Total efficiency in DM ALP signals couples the combined efficiency of Fig. 2 with the selected analysis threshold at 325 eV. Their variations with the DM ALP mass are depicted in Fig. 8(a). Constraints on g_{Ae} for the DM ALP mass between 0.5 and 20 keV/c^2 are derived with the unbinned maximum likelihood method. The best-fit ALP-induced recoil spectrum at a mass of 0.5 keV/c^2 is depicted in Fig. 3. Below 0.5 keV/c^2, no background subtraction is applied, and the upper bounds on g_{Ae} correspond to those where the ALP-induced rates do not exceed the observed ones at 90% C.L. The efficiency-corrected background spectra are displayed in Fig. 8(b), where the data above 475 eV with BSD and below 475 eV without BSD are adopted. The excluded spectra at an ALP mass of 250, 300, and 400 eV/c^2 are superimposed. The 90% C.L. limit on g_{Ae} is displayed in Fig. 9. The peaks in the limit plots correspond to the K/L x-ray peaks in the spectrum, and the steps around 1.3 and 10 keV are due to the atomic energy levels. Because of the monochromatic signal and the good energy resolution, the limit is sensitive to the fluctuations of individual bins. The CDEX-1 limits are more stringent than the results from CoGeNT [13] at a mass less than 1 keV, due to the improved detector threshold, energy resolution, and residual background.

V. SUMMARY AND PROSPECTS

We present results on solar and DM ALPs searches with CDEX-1 data in this article. Point-contact germanium detectors, with their low-energy threshold and excellent energy resolution to be able to resolve spectral structures like peaks, are particularly suited for the studies of axions and ALPs.

Further improvement on experimental sensitivities is being pursued by the CDEX-1 experiment. At a benchmark detector threshold of 100 eV, a background of 1 kg^{-1} keV^{-1} day^{-1}, and an exposure of 1 kg year [52], DM ALPs can be probed down to a mass of 100 eV at g_{Ae} of 7×10^{-13}.

ACKNOWLEDGMENTS

This work was supported by the National Natural Science Foundation of China (Contracts No. 11505101, No. 11175099, No. 11275107, No. 11475117, and No. 11475099), the National Basic Research Program of China (973 Program) (2010CB833006), China Postdoctoral Science Foundation (2015M581063), MOST 104-2112-M-001-038-MY3, and the Academia Sinica Principle Investigator Award 2011–2015 from Taiwan.

[1] C. A. Baker *et al.*, Phys. Rev. Lett. **97**, 131801 (2006).
[2] R. D. Peccei and H. R. Quinn, Phys. Rev. Lett. **38**, 1440 (1977); Phys. Rev. D **16**, 1791 (1977).
[3] S. Weinberg, Phys. Rev. Lett. **40**, 223 (1978).
[4] F. Wilczek, Phys. Rev. Lett. **40**, 279 (1978).
[5] J. E. Kim, Phys. Rep. **150**, 1 (1987); Rev. Mod. Phys. **82**, 557 (2010).
[6] A. Ringwald, Phys. Dark Univ. **1**, 116 (2012).
[7] M. Dine, W. Fischler, and M. Srednicki, Phys. Lett. B **104**, 199 (1981).
[8] A. R. Zhitniskiy, Yad. Fiz. **31**, 497 (1980).
[9] J. E. Kim, Phys. Rev. Lett. **43**, 103 (1979).
[10] M. A. Shifman, A. I. Vainshtein, and V. I. Zakharov, Nucl. Phys. **B166**, 493 (1980).
[11] Z. Ahmed *et al.*, Phys. Rev. Lett. **103**, 141802 (2009).

[12] R. Bernabei *et al.*, Phys. Lett. B **515**, 6 (2001).

[13] C. E. Aalseth *et al.*, Phys. Rev. Lett. **106**, 131301 (2011).

[14] F. Alessandria *et al.*, J. Cosmol. Astropart. Phys. 05 (2013) 007.

[15] E. Armengaud *et al.*, J. Cosmol. Astropart. Phys. 11 (2013) 067.

[16] K. Abe *et al.*, Phys. Lett. B **724**, 46 (2013).

[17] E. Aprile *et al.*, Phys. Rev. D **90**, 062009 (2014).

[18] E. Aprile *et al.*, Phys. Rev. D **95**, 029904(E) (2017).

[19] M. Arik *et al.*, Phys. Rev. Lett. **107**, 261302 (2011).

[20] G. Rybka, Phys. Dark Univ. **4**, 14 (2014).

[21] K. A. Olive *et al.*, Chin. Phys. C **38**, 090001 (2014).

[22] M. Schumann, Eur. Phys. J. Web Conf. **96**, 01027 (2015).

[23] P. Cushman *et al.*, arXiv:1310.8327.

[24] A. S. Barabash, Phys. Procedia **74**, 416 (2015); AIP Conf. Proc. **1686**, 020003 (2015).

[25] S. M. Bilenky and C. Giunti, Mod. Phys. Lett. A **27**, 1230015 (2012); S. R. Elliott, Mod. Phys. Lett. A **27**, 1230009 (2012).

[26] K. J. Kang *et al.*, Front. Phys. **8**, 412 (2013).

[27] K. J. Kang, J. P. Cheng, Y. H. Chen, Y. J. Li, M. B. Shen, S. Y. Wu, and Q. Yue, J. Phys. Conf. Ser. **203**, 012028 (2010).

[28] Y. C. Wu *et al.*, Chin. Phys. C **37**, 086001 (2013).

[29] S. K. Liu *et al.*, Phys. Rev. D **90**, 032003 (2014).

[30] H. Jiang *et al.*, Chin. Phys. C **40**, 096001 (2016).

[31] W. Zhao *et al.*, Phys. Rev. D **88**, 052004 (2013).

[32] Q. Yue *et al.*, Phys. Rev. D **90**, 091701(R) (2014).

[33] W. Zhao *et al.*, Phys. Rev. D **93**, 092003 (2016).

[34] K. Barth *et al.*, J. Cosmol. Astropart. Phys. 05 (2013) 010.

[35] J. Redondo, J. Cosmol. Astropart. Phys. 12 (2013) 008.

[36] W. C. Haxton and K. Y. Lee, Phys. Rev. Lett. **66**, 2557 (1991).

[37] S. Moriyama, Phys. Rev. Lett. **75**, 3222 (1995).

[38] S. Andriamonje *et al.*, J. Cosmol. Astropart. Phys. 12 (2009) 002.

[39] D. B. Kaplan, Nucl. Phys. **B260**, 215 (1985).

[40] M. Srednicki, Nucl. Phys. **B260**, 689 (1985).

[41] A. M. Green, Mod. Phys. Lett. A **27**, 1230004 (2012).

[42] F. Alessandria *et al.*, J. Cosmol. Astropart. Phys. 05 (2013) 007.

[43] A. Derevianko, V. A. Dzuba, V. V. Flambaum, and M. Pospelov, Phys. Rev. D **82**, 065006 (2010).

[44] M. Pospelov, A. Ritz, and M. Voloshin, Phys. Rev. D **78**, 115012 (2008).

[45] H. B. Li *et al.*, Phys. Rev. Lett. **110**, 261301 (2013); Astropart. Phys. **56**, 1 (2014).

[46] G. COWAN, *Statistical Data Analysis* (Oxford University, New York, 1998).

[47] P. Gondolo and G. G. Raffelt, Phys. Rev. D **79**, 107301 (2009).

[48] N. Viaux, M. Catelan, P. B. Stetson, G. G. Raffelt, J. Redondo, A. A. R. Valcarce, and A. Weiss, Phys. Rev. Lett. **111**, 231301 (2013).

[49] G. G. Raffelt, Lect. Notes Phys. **741**, 51 (2008).

[50] D. Adams *et al.*, Phys. Rev. D **56**, 5330 (1997).

[51] G. Altarelli, R. D. Ball, S. Forte, and G. Ridolfi, Nucl. Phys. **B496**, 337 (1997).

[52] Q. Yue, K. J. Kang, J. M. Li, and H. T. Wong, J. Phys. Conf. Ser. **718**, 042066 (2016).